TU/e EINDHOVEN UNIVERSITY OF TECHNOLOGY

A model for the diffusion and precipitation of antimony in highly doped δ layers in silicon

Citation for published version (APA):
van Opdorp, C., van IJzendoorn, L. J., Fredriksz, C. W., & Gravesteijn, D. J. (1992). A model for the diffusion and precipitation of antimony in highly doped δ layers in silicon. *Journal of Applied Physics*, *72*(9), 4047-4062. https://doi.org/10.1063/1.352338

DOI:
10.1063/1.352338

Document status and date:
Published: 01/12/1992

Document Version:
Publisher's PDF, also known as Version of Record (includes final page, issue and volume numbers)

Please check the document version of this publication:

• A submitted manuscript is the version of the article upon submission and before peer-review. There can be important differences between the submitted version and the official published version of record. People interested in the research are advised to contact the author for the final version of the publication, or visit the DOI to the publisher's website.
• The final author version and the galley proof are versions of the publication after peer review.
• The final published version features the final layout of the paper including the volume, issue and page numbers.

Link to publication

General rights
Copyright and moral rights for the publications made accessible in the public portal are retained by the authors and/or other copyright owners and it is a condition of accessing publications that users recognise and abide by the legal requirements associated with these rights.

• Users may download and print one copy of any publication from the public portal for the purpose of private study or research.
• You may not further distribute the material or use it for any profit-making activity or commercial gain
• You may freely distribute the URL identifying the publication in the public portal.

If the publication is distributed under the terms of Article 25fa of the Dutch Copyright Act, indicated by the “Taverne” license above, please follow below link for the End User Agreement:

www.tue.nl/taverne

Take down policy
If you believe that this document breaches copyright please contact us at:

openaccess@tue.nl

providing details and we will investigate your claim.

Download date: 05. Oct. 2023

A model for the diffusion and precipitation of antimony in highly doped δ layers in silicon

C. van Opdorp, L. J. van IJzendoorn, C. W. Fredriksz, and D. J. Gravesteijn

Citation: Journal of Applied Physics 72, 4047 (1992); doi: 10.1063/1.352338
View online: https://doi.org/10.1063/1.352338
View Table of Contents: http://aip.scitation.org/toc/jap/72/9
Published by the American Institute of Physics

AIP | Journal of Applied Physics SPECIAL TOPICS

A model for the diffusion and precipitation of antimony in highly doped δ layers in silicon

C. van Opdorp, L. J. van IJzendoorn,[a] C. W. Fredriksz, and D. J. Gravesteijn[b]
Philips Research Laboratories, 5600 JA Eindhoven, The Netherlands

(Received 20 April 1992; accepted for publication 17 July 1992)

Antimony δ-doping layers were made by deposition of Sb on monocrystalline Si, followed by the deposition of amorphous Si and a final solid-phase-epitaxy treatment at 620 °C. After post-annealing at temperatures between 625 and 725 °C, Sb precipitates with a diameter of several nm are observed in the δ plane with the aid of transmission electron microscopy. Using channeling Rutherford Backscattering Spectrometry the increase of the precipitated fraction with time was determined from the minimum-yield signal. The results are interpreted using a model for the generation of Sb nuclei which grow subsequently due to lateral diffusion of Sb atoms in the δ plane, followed by incorporation into the nucleus. The generation of the nuclei appears to take place by way of two parallel processes: (i) fast, simultaneous generation of a limited number of nuclei at low-energetic sites in the δ plane, with subsequent diffusion-controlled growth, and (ii) slow, continuous generation of a larger number of nuclei at random sites in the δ plane, with subsequent incorporation-controlled growth. The Sb diffusion at the extremely high concentrations under consideration is very fast and concentration dependent, which can be explained by the model of vacancy-percolation diffusion of Mathiot and Pfister [J. Appl. Phys. **66**, 970 (1989)]. The activation energy for incorporation of Sb atoms into liquid precipitates appears to be considerably lower than for incorporation into solid ones.

I. INTRODUCTION

Impurity doping in a single atomic plane of semiconductor material has a large number of potential device applications; see, e.g., Ref. 1. A well-known example is the antimony δ-doping layer in silicon.[1–15] In a previous paper[16] we reported on the thermal stability of such layers which were fabricated by deposition of Sb on a monocrystalline Si substrate, followed by the deposition of amorphous Si and a final solid-phase-epitaxy (SPE) treatment at 620 °C. These layers, which contained 3.1×10^{14} Sb atoms per cm^2 (approximately $\frac{1}{2}$ monolayer), exhibited precipitation under post annealing. This behavior is of practical interest with a view to device processing steps subsequent to the realization of the δ layer.

The results of Ref. 16 are briefly summarized in this paragraph. Using cross-sectional transmission electron microscopy (XTEM) we showed that Sb precipitation took place in spheres with a diameter of several nm, situated in the δ-doping plane. The δ layers had been investigated further systematically with Rutherford backscattering spectrometry (RBS) before and after the successive annealing steps at temperatures between 625 and 725 °C. An example of a random and a channeled RBS spectrum is given in Fig. 1. The number of Sb atoms per unit of area in the δ-doping layer as evaluated from the Sb peak area in the random spectrum. Channeled RBS spectra were measured by aligning the incoming ion beam with the [100] axis of the silicon crystal. In that case Sb atoms located at substitutional sites are shielded from the incoming ion beam. Thus, from the Sb peak area in the channeled spectrum one can calculate the number of Sb atoms at nonsubstitutional sites, which was taken to be that in the precipitates. Furthermore, within the RBS depth resolution of 7 nm we found no effects of perpendicular Sb diffusion (in agreement with the observations for the same temperature range in Refs. 9 and 10), from which we concluded that lateral Sb diffusion within the δ plane rather than diffusion away from the δ plane is the dominating transport process.[17]

Observation of Sb precipitation in supersaturated silicon had already been reported by other investigators, both for δ-layer-doped[11–13,15] and three-dimensional-doped silicon.[18–29] The δ layers of Refs. 11–13 and 15 were prepared by a method analogous to ours, while the three-dimensional (3D) doping regions in Refs. 18–29 were established by high-energetic Sb-ion implantation with subsequent annealing for removing the damage thus introduced. Interpreting the observed dependence of the RBS minimum-yield signal of δ layers on annealing time and temperature in terms of lateral transport followed by precipitation can provide more information on the underlying mechanisms. We already presented rough outlines of a model based on such considerations in Ref. 16. In the present paper a more extended and quantitative analysis and model will be given.

In Refs. 30–32 it was already found that in 3D cases the diffusion coefficient D of Sb can be more than a decade higher than expected from extrapolating the model of Fair, Manda, and Wortman.[33] According to this model, for Sb concentrations C near 2×10^{20} cm^{-3} D varies with C as $D=D_0C^2$. Extrapolation of this equation to the concentrations in question, i.e., up to 7×10^{20} cm^{-3}, produced the mentioned considerable underestimate. Actually, it has

[a]Present address: Eindhoven University of Technology, Cyclotron Laboratory 1.17, P.O. Box 513, 5600 MB Eindhoven, The Netherlands.
[b]Author to whom correspondence should be addressed.

 © 1992 American Institute of Physics

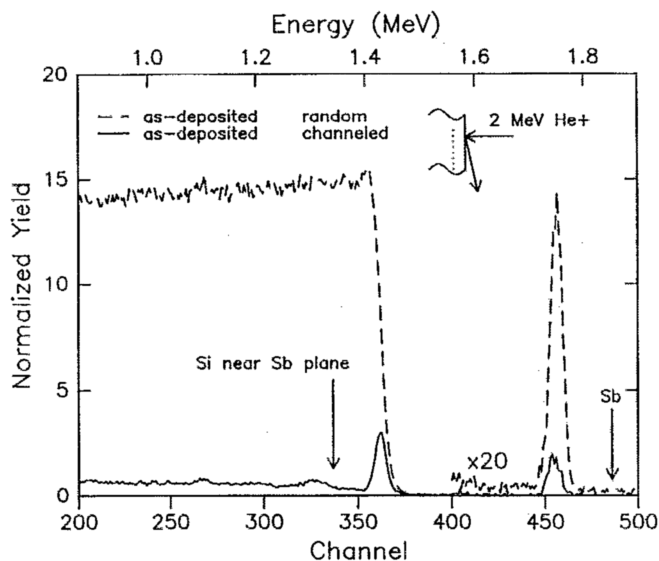

FIG. 1. Example of 2 MeV He^+ RBS spectra of an as-deposited Sb δ-doping layer, measured with a scattering angle of 100°. The integrated random Sb yield corresponds to 3.1×10^{14} atoms per cm^2. (From Ref. 16.)

been reported.[3,30,31,34] that D in this C range can be described phenomenologically by $D=D_0C^s$ with variable s. At 1050 °C, for example, s increases from 1.7 to 3.6 when C increases from 1×10^{20} to 3×10^{20} cm^{-3}.

A provisional estimate of D in our δ layers also points to very high values. This estimate follows from equating the time t after which the RBS minimum-yield signal has become practically constant (indicating the end of the precipitation) with r_0^2/D. Here r_0 represents the extent of the region which has been depleted of Sb atoms above the solid-solubility limit, for which extent we take half the average mutual distance between the precipitates. For 650 °C we thus found[16]

$$D\approx r_0^2/t\approx4\times10^{-12}/2\times10^3=2\times10^{-15}\ cm^2/s,$$

whereas extrapolating Fair's equation gives only 2.5×10^{-17} cm^2/s (see Sec. V A).

An interpretation for the observed strong increase of D with C in 3D has been given by Mathiot and Pfister[35-38] and more recently by Larsen *et al.*[32,39] in terms of percolation theory. Just like Fair, Manda, and Wortman,[33] for not too high C values these authors start from considering the diffusing species as partially dissociating complexes of an impurity atom and a (charged) lattice vacancy.[40,41] They remark, however, that this concept of basically noninteracting complexes becomes invalid at very high impurity concentrations C. It is claimed that an adequate description of the diffusion of various impurities in Si is possible by introducing a "percolation diffusivity" D_{perc}. This D_{perc} starts to play a decisive role rather abruptly when C exceeds the "percolation threshold" C_{perc} above which the fraction of the impurities which occupy fifth-neighboring sites in the Si lattice passes a certain critical value. Above this critical value there is a finite probability for the existence of an interconnected fifth-neighbor impurity network extending throughout the whole lattice. The authors argue that impurity-vacancy complexes in this network can *completely* dissociate quite easily then, the vacancy thus being able to percolate practically freely through the whole network. This easy diffusion path for vacancies opens up an equally easy diffusion path for the impurities themselves by way of the usual interchange of sites with the vacancies, without forming now, however, stable complexes. Moreover, above the percolation threshold the diffusivity is further increased by a decrease of the formation enthalpy of the vacancies, again due to fifth-neighbor interactions.

In our view this "vacancy-percolation model" provides as yet also the best available conceptual framework for comprehending the very fast 2D diffusion of a number of impurities in Si at very high concentrations. Adopting the main lines of the 3D model for the Sb δ layers can explain characteristic features of our RBS data. This does not imply, however, that we are endorsing quantitative claims like those made in Refs. 32 and 35–39. These claims and our objections will be phrased in Sec. V A.

Apart from the phenomenon of very fast diffusion, the analysis of our RBS data in the present paper indicates that two types of precipitates develop in the δ plane. These have significantly different sizes and thermal activation energies of growth rates. First, there are the precipitates with roughly identical diameters which are visible on the TEM pictures. All of them are already present directly after the SPE treatment; during the subsequent annealing, diffusion-controlled growth of these precipitates occurs. Second, there is strong evidence that continuous nucleation of still another type of precipitates is taking place simultaneously. These remain supposedly too small here (diameter <1 nm) for unambiguous observation by TEM. Due to these small sizes the Sb transport to the latter type of precipitates is incorporation controlled.

The organization of this paper is as follows. In Sec. II the preparation procedures and the full results of the TEM and RBS measurements are given. Section III presents our model, which is applied to the experimental data in Sec. IV. The discussion is given in Sec. V, while Sec. VI presents the conclusions.

II. EXPERIMENTAL PROCEDURES AND RESULTS

Sb-doped δ layers have been grown on (100)-oriented 4-in.-diam. Si substrates of p-type ($\rho>10^3$ Ω cm) floating-zone material. In a first step the residual oxide on the substrate was thermally evaporated *in situ*. Then a 100-nm-thick Si buffer layer was grown under standard conditions at a substrate temperature of 700 °C, using the technique of molecular beam epitaxy (MBE). Details of the MBE system have been reported elsewhere.[42] Subsequently, a layer of 3.1×10^{14} Sb-atoms per cm^2 was deposited from a Knudsen cell. [A full monolayer on a (100) Si plane contains 6.78×10^{14} Sb-atoms per cm^2.] After cooling down to room temperature, a 50-nm amorphous Si layer was deposited. Finally, this top layer was crystallized epitaxially by ramping up the temperature to 620 °C in approximately 15 min.

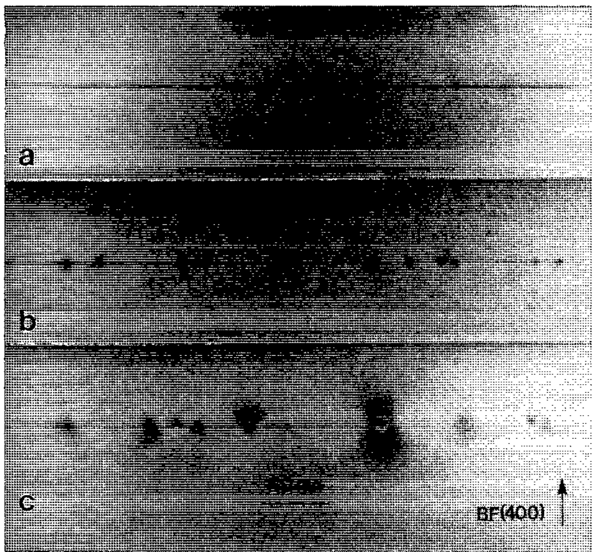

FIG. 2. Cross-sectional TEM micrographs of an Sb δ-doping layer after different annealing times t at 650 °C; (a) $t=0$ s, (b) $t=900$ s, and (c) $t=3600$ s.

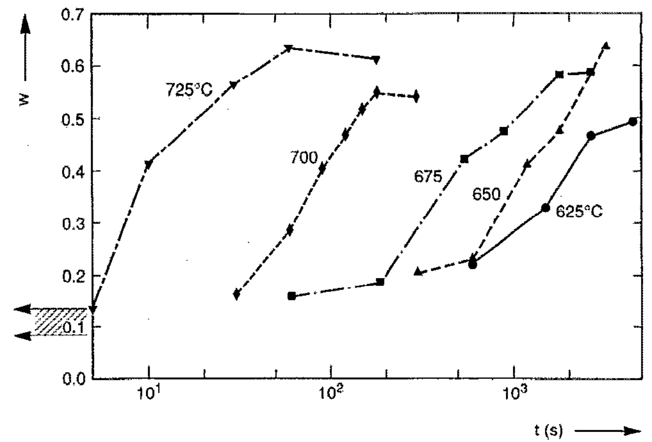

FIG. 3. Semilogarithmic plot of the precipitated fraction W of Sb atoms vs the annealing time t, for different annealing temperatures. The values of W were calculated from Eq. (2). The W values for $t=0$ s are situated within the hatched interval.

A number of samples were cut from one of the above wafers, after which annealing experiments were carried out in the target chamber of the RBS facility. Details of the heating method, the temperature measurements and the RBS technique, as well as the results, can be found in Ref. 16. Channeling RBS spectra were measured while the samples were at ambient temperature, after annealing at 625, 650, 675, 700, and 725 °C. The depth resolution was limited by energy straggling to approximately 7 nm. TEM pictures were taken with a Philips EM 400T microscope using 120-keV electrons. Cross-sectional $\langle 110 \rangle$ images were taken by diffraction on the (400) planes in bright field.

Figure 2(a) shows the TEM image of an as-deposited sample. Precipitates in the δ-doping plane already show up here. Figures 2(b) and 2(c) show the TEM cross sections after annealing at 650 °C for 900 and 3600 s, respectively. Corresponding plan-view pictures revealed a practically time-independent density of precipitates of roughly 6×10^{10} cm^{-2}. High-resolution TEM pictures revealed that the precipitates are monocrystalline, but have random orientations with respect to the Si lattice. From x-ray reflection measurements on a 0.9 monolayer Sb δ-doped sample the thickness h of the δ layers was found to be $h \approx 1.3$ nm.[43] From the random RBS spectra (cf. Fig. 1) it was concluded that no Sb was lost during the experiments and that all Sb remains in the δ plane.

The fraction W of the Sb atoms in the precipitates was calculated as follows. The minimum yield $\chi_{\min}(\mathrm{imp})$ of an impurity in a given host lattice is defined as the ratio of the yields in the channeled and in a random RBS spectrum. The same ratio measured for the host atoms in a sample without impurities is denoted by $\chi_{\min}(\mathrm{host})$. A first-order estimate of the substitutional fraction S of the impurity is given then by[44]

$$S=\frac{1-\chi_{\min}(\mathrm{imp})}{1-\chi_{\min}(\mathrm{host})}. \quad (1)$$

Equating W to the fraction of nonsubstitutional Sb atoms, $1-S$, we find

$$W=\frac{\chi_{\min}(\mathrm{Sb})-\chi_{\min}(\mathrm{Si})}{1-\chi_{\min}(\mathrm{Si})}. \quad (2)$$

Our W values were calculated from this equation using $\chi_{\min}(\mathrm{Si})=0.03$.[42]

A plot of W vs $\ln t$ for the different annealing temperatures is given in Fig. 3. In such a plot the W values for $t=0$ cannot be represented; these are included in the double-linear plots of Fig. 4. In these plots we have omitted the data points of the longest (or two longest) annealing times. The suggestive curves drawn in Fig. 4 will come up for discussion in the next section.

III. THE PRECIPITATION MODEL

A. Evidence for two parallel precipitation processes

When the data points of each series in Fig. 4 are connected with straight-line elements, a salient feature in all of them—except the 625 °C series—is the occurrence of a kink near the second or third point. We have found similar kinks for samples cut from Sb δ layers containing 5.4×10^{14} Sb atoms per cm^2. The persistence of this feature makes the existence plausible of a similar kink in the 625 °C curve of Fig. 4, presumably between the second and third point. Since W cannot exceed unity, the general trend for the highest points is a concave shape. The three lowest points of the 650 and 675 °C series of Fig. 4 also reveal a concave interval; again it is plausible that this is the general initial shape for all five samples.

The overall general shape of the $W-t$ curve thus consists of two concave intervals, I and II, separated by a kink. Such a shape strongly suggests an assignment to two parallel precipitation processes. This is illustrated schemati-

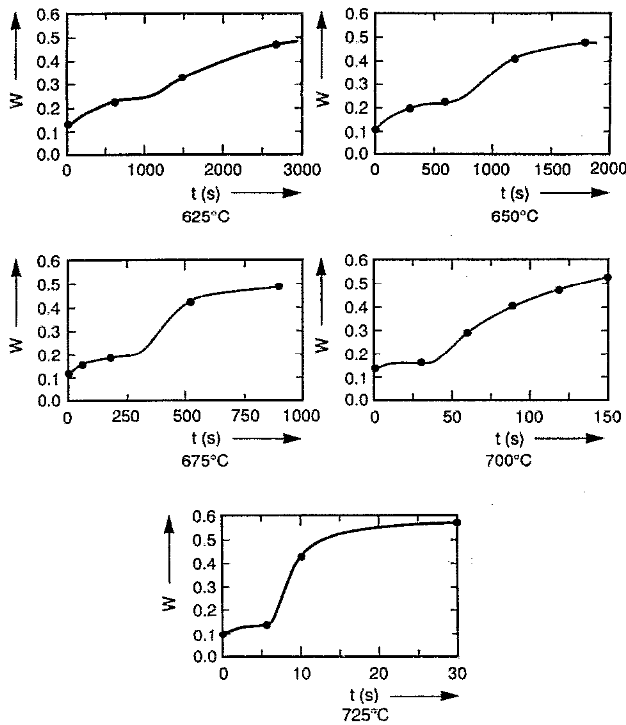

FIG. 4. The data of Fig. 3, including the data for $t=0$ s, in double-linear plots. The data points of the (two) longest annealing time(s) have been omitted here. The suggestive curves serve merely as a guide to facilitate the discussion in the first paragraph of Sec. III A, and have no quantitative meaning.

cally in Fig. 5: a concave curve $W_{\mathrm{I}}(t)$ saturating roughly at $W \approx 0.2$, and a slower-starting sigmoid curve $W_{\mathrm{II}}(t)$ saturating at a higher W value. The idea of two different parallel processes is further corroborated by the appearance of

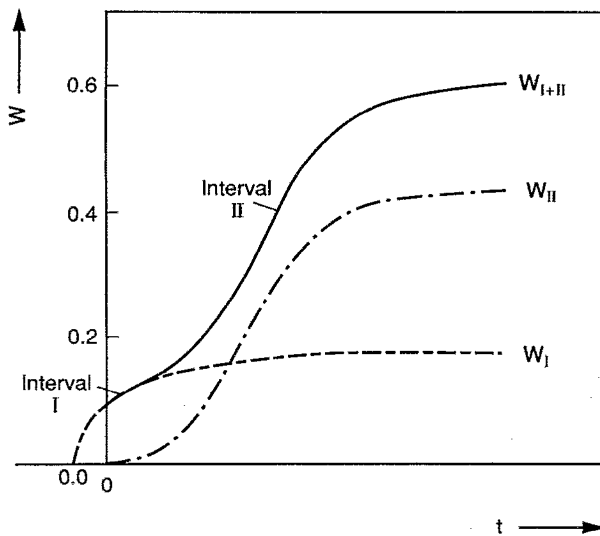

FIG. 5. Schematic $W-t$ curve representative for the general shape of the data of Fig. 4 (solid line). The presence of two separate concave intervals, I and II, suggests the assignment of the overall precipitation $W_{\mathrm{I+II}}(t)$ to two different parallel processes (chain lines). Note that $W_{\mathrm{I+II}}(t) \neq W_{\mathrm{I}}(t) + W_{\mathrm{II}}(t)$; cf. Eq. (27).

different thermal activation energies in the intervals I and II, as will be demonstrated now.

A possible approach for studying activation energies consists in making horizontal cross sections through the curves of Fig. 3 or 4; the time intervals needed for establishing a given value of W at the five different temperatures are plotted then in an Arrhenius plot of $\ln(1/t)$ vs $1/T$. The relevance of such an approach is demonstrated most easily for a first-order process with a single activation energy E. In such a process the fraction of non-precipitated material Γ ($\equiv C/C_{\mathrm{in}}$, where C_{in} is the initial value of C) decreases as $d\Gamma/dt = -\Gamma/\tau$. Here τ is a time constant which can be expressed in the parameters of the underlying physical mechanisms, and which generally depends on T as $\tau = \tau_A \exp(E/kT)$ [cf. Eq. (35)], where τ_A is a constant and k is the Boltzmann constant. Solving the differential equation for Γ yields for W:

$$W = 1 - \Gamma = 1 - \exp(-t/\tau). \tag{3}$$

Thus for constant W one has $\ln(1/t) = B - E/kT$, with the constant B given by

$$B \equiv -\ln[\tau_A \ln(1-W)^{-1}].$$

In more complex cases the dependence of W on t may still be given by a function of t/τ with a single τ, but this function $W(t/\tau)$ will be more complicated than that of Eq. (3); cf. Eqs. (9), (18), and (24). Knowledge of the particular function in question is, however, not necessary for evaluating E: provided that the dependence of τ on T is still given by an exponential expression like that directly preceding Eq. (3), the $\ln(1/t) - 1/T$ plots for different W-values will still produce parallel straight lines having a slope corresponding to the same, single E value. One needs to know the functional form $W(t/\tau)$ only for possible evaluation of the constant τ_A. We shall start here by making the suggested $\ln(1/t) - 1/T$ plots; the derivation of the pertinent theoretical function $W(t/\tau)$ will be postponed to Sec. III B.

Our $\ln(1/t) - 1/T$ plots for nine values of W are presented in Fig. 6. The t values were obtained from Fig. 3; only for the low W values that gave no point of intersection there, Fig. 4 was used instead. At first sight the results are not encouraging. Though the curves for $W \geqslant 0.25$ (the type II interval) are nearly parallel, as anticipated, they are not straight. The curves for $W \leqslant 0.18$ (the type I interval) are even far from parallel. This difference between the two groups of curves supports the idea of two different precipitation mechanisms dominating below and above the kinks in the curves of Fig. 4. By elaborating this idea one can bring more order in the curves of Fig. 6 and grasp their physical sense.

It will be shown that the type I intervals of the curves in Fig. 4 are attributable to diffusion-controlled growth of the relatively large precipitates with approximately identical diameters visible on the TEM pictures of Fig. 2. Though the larger precipitates exhibit a lens shape, in our simplified model they will be considered as spherical. The type II intervals will be attributed tentatively to much smaller spheres, *not* visible on the TEM pictures, with

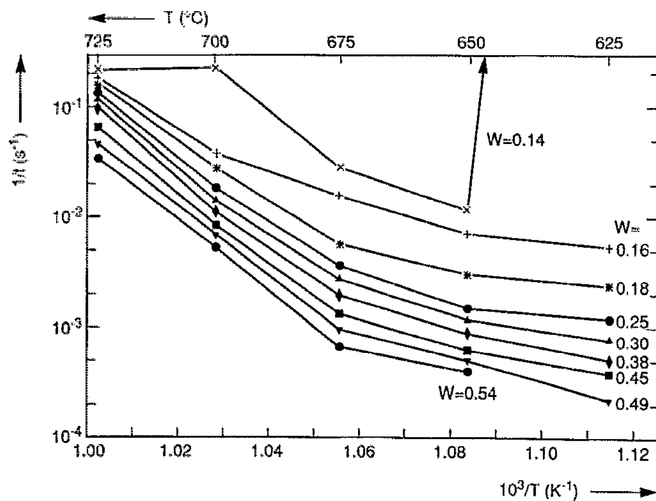

FIG. 6. Arrhenius plots for the $1/t$ values obtained from horizontal cross sections through Figs. 3 and 4, for various values of W. The $W=0.14$ plot is very inaccurate.

varying diameters and much higher density. In order to allow such attributions, we shall need the preliminary theoretical elaborations of the next sections. On the other hand, the TEM pictures do *not* allow quantitative estimating of the amount of Sb in the larger spheres and consequently equally not of the division of W over the two types of precipitates.

B. Sequential stages in precipitation

When considering a single precipitation process (i.e., without any parallel process), in the course of time one can generally distinguish a nucleation and a growth stage. In conformity with the terminology for precipitation in 3D, in our 2D case we shall make use of the terms heterogeneous and homogeneous nucleation with a duly adapted sense. "Heterogeneous nucleation" will denote here the formation of nuclei of Sb atoms at low-energetic sites (not further specified here) in the δ plane; "homogeneous nucleation" will refer to nucleation at numerous random non-low-energetic lattice sites in the same δ plane, due to statistical density fluctuations of the Sb atoms occasionally producing supercritical nuclei.

Once the radius R of a nucleus has managed to surpass a certain critical value R_c, the growth stage proper starts (for $R<R_c$ there is still a large chance of dissolution of the subcritical nucleus; see, e.g., Refs. 45–47.) During this growth stage two processes are acting in series: transport of Sb atoms by diffusion to the precipitate surface, followed by their incorporation into the precipitate. For sufficiently low values of R the incorporation process is always rate-limiting, since the diffusion-determining concentration gradient at the surface varies inversely with R [cf. Appendix B, Eq. (B7)]. Thus one can generally distinguish three subsequent stages in the development of a given precipitate: nucleation, incorporation-controlled growth and diffusion-controlled growth. In general there may follow still another stage, viz. that of Ostwald ripening. During this final stage larger precipitates grow at the expense of smaller ones, which disappear eventually. This leads to a reduction of the number of precipitates, typically with many orders of magnitude, while the value of W usually remains virtually invariant.[48]

In view of the foregoing, when considering now the collection of all precipitates resulting from a single precipitation process one can distinguish two possible cases: (1) all supercritical nuclei have been formed virtually at the same moment, so that their number remains further constant, and (2) supercritical nuclei are being formed continuously. The former case is usually correlated with heterogeneous nucleation, where the nucleation at the low-energetic sites is so fast that these sites are saturated within a very short period. Case (2) is often, though not exclusively, ascribable to the much slower, nonsaturating homogeneous nucleation.

In Sec. IV it will be shown that the two parallel processes that can explain our experimental data start with nucleation processes of the above types (1) and (2). In order to justify these assignments, we have to firstly derive the mathematical formulations for the increase of W vs t for the two cases separately. These functions will be denoted henceforth as $W_1(t)$ and $W_2(t)$.

In deriving $W_1(t)$ and $W_2(t)$, the Sb diffusion perpendicular to the δ plane will be completely neglected in view of the extremely small D in the undoped material outside the δ layer. This can be justified by calculating the penetration depth x^* for perpendicular diffusion in the case that D can be described by $D=D_0C^s$. Here x^* is defined as the depth at which the Sb concentration C in the originally undoped material has increased to an arbitrarily chosen value. Without actually solving the pertinent one-dimensional partial differential equation for the diffusion, it can be shown rather easily that x^* increases with t as a certain function of $t^{1/(s+2)}$. Consequently, for our very high values of $s(s\approx 25$; see Sec. IV A), x^* is expected to generally increase only very slowly with t.

1. Type (1): The growth of simultaneously generated nuclei

We shall treat the incorporation- and diffusion-controlled cases separately.

a. Incorporation-controlled growth. We suppose that all supercritical nuclei have been generated simultaneously at $t=0$ with a density n per unit of area in the δ plane. In describing the ensuing incorporation-controlled growth we shall consider spherical precipitates that protrude relatively far beyond the extremely thin δ layer. We denote the sphere radius by R and the concentration of Sb atoms per unit of volume in the δ layer by C, with the initial value C_{in}. In the direction perpendicular to the δ plane we postulate a rectangular-shaped Sb-concentration profile with the invariant thickness h.

For a given precipitate the incorporation of Sb atoms takes place over a ring-shaped surface with area $2\pi Rh$. Assuming a first-order interfacial reaction process, the number of Sb atoms which is incorporated per unit of time into the precipitate equals

$$2\pi Rkh(C-C_s)\approx 2\pi RkhC.$$

Here C_s is the solid-solubility limit and k is the surface-reaction-rate coefficient with the dimension of velocity, and of the form

$$k=k_A \exp(-E_{\rm surf}/kT). \tag{4}$$

After crossing the ring-shaped surface, the Sb atoms will rearrange themselves over the precipitate, trying to maintain a spherical surface of minimum free energy. The fast self-diffusion in metallic Sb (see Sec. V A) favors fast rearranging. In addition to this, however, a spherical shape requires easy displaceability of Si atoms adjoining the whole precipitate surface. The vacancies enabling this displacement are mainly supplied by the δ layer: within this layer both the concentration and the diffusion coefficient of negatively charged vacancies are very high (cf. the paragraph summarizing the vacancy-percolation theory in Sec. I). Fast transport of vacancies from the ring-shaped surface to other parts of the precipitate surface may take place through the (liquid) bulk of the precipitate. A possible alternative vacancy-supply road is a very thin Si shell directly adjoining the precipitate surface. An n-type inversion layer may exist here between the metallic Sb precipitate and the p-type Si. In such a layer—just as in the δ layer, though in a lesser degree—the equilibrium concentration of negative vacancies is greatly enhanced with respect to the surrounding p-type Si.

The fact that the larger precipitates in Fig. 2(c) exhibit a lens shape rather than a spherical one might indicate that the rearrangement of Sb atoms cannot entirely keep pace with their supply. Assuming nevertheless a spherical shape for all precipitates, the incorporation-controlled rate of volume growth of a sphere is given by

$$\frac{dV}{dt}=\frac{d}{dt}\left(\frac{4\pi R^3}{3}\right)=2\pi RvkhC, \tag{5}$$

where v is the atomic volume of Sb. Integrating the first as well as the second of Eqs. (5), combining the results, and making use of $R(0)=R_c\approx 0$ [which is allowed for all $R(t)\gg R_c$], yields for the time dependence of the sphere volume:

$$V(t)=\frac{4\pi}{3}R^3(t)=\frac{4\pi}{3}\left(vkh\int_0^t C(t')\,dt'\right)^{3/2}. \tag{6}$$

Substituting here $C(t)=C_{\rm in}[1-W_1^i(t)]$, where the lower index 1 of W_1^i refers to the type (1) nucleation process and its upper index i to the incorporation-controlled growth regime, this becomes

$$V(t)=\frac{4\pi}{3}R^3(t)=\frac{4\pi}{3}\left(vkhC_{\rm in}\int_0^t [1-W_1^i(t')]dt'\right)^{3/2}. \tag{7}$$

Thus we obtain for $W_1^i(t)$:

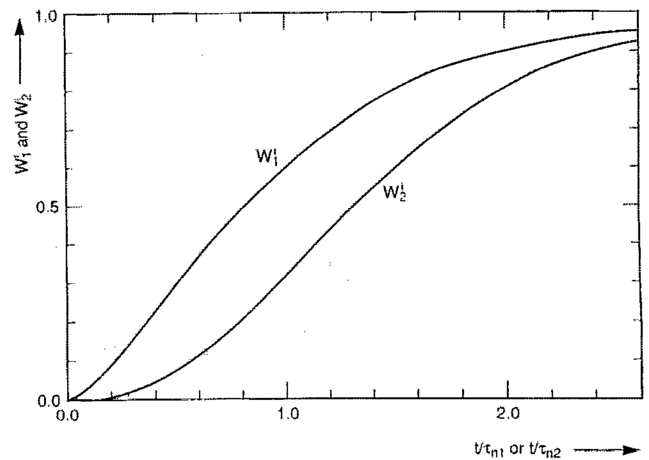

FIG. 7. The incorporation-controlled growth stage of precipitates: theoretical curves of the precipitated Sb fractions W_1^i and W_2^i vs the normalized annealing time. The lower index refers to either of the following nucleation processes: (1) simultaneous (heterogeneous) generation of nuclei—see Eqs. (9)–(11); (2) continuous (homogeneous) generation of nuclei—see Eqs. (24)–(26).

$$W_1^i(t)=\frac{nV(t)}{vhC_{\rm in}}=\frac{4\pi}{3}nk^{3/2}(vhC_{\rm in})^{1/2}\times\left(\int_0^t [1-W_1^i(t')]dt'\right)^{3/2}. \tag{8}$$

This can be rewritten in the dimensionless form:

$$W_1^i(\mathscr{T}_1)=\left(\int_0^{\mathscr{T}_1} [1-W_1^i(t')]dt'\right)^{3/2}, \tag{9}$$

where $\mathscr{T}_1$ is defined as

$$\mathscr{T}_1\equiv t/\tau_{n1} \tag{10}$$

with the time constant τ_{n1} given by

$$\tau_{n1}\equiv\frac{1}{k}\left[\left(\frac{3}{4\pi n}\right)^2\frac{1}{vhC_{\rm in}}\right]^{1/3}. \tag{11}$$

The nonlinear integral equation (9) cannot be solved analytically. The result of the numerical solution obtained in Appendix A is shown in Fig. 7.

b. Diffusion-controlled growth. When the radii R have become sufficiently large, the further growth of the spheres becomes practically exclusively determined by the diffusional supply of the Sb-atoms through the δ layer. As stated in Sec. I, we shall adopt the vacancy-percolation model for describing the diffusion at our extremely high Sb concentrations. For the moment we follow the heuristic approach of describing D very roughly by

$$D=D_0C^s \tag{12}$$

with

$$D_0=D_{0A}\exp(-E_{\rm diff}/kT). \tag{13}$$

In these as well as in all our other equations the index 0 denotes independence of C, while A denotes independence of T. Note that D and D_0 have different dimensions. In Eq.

(12) we shall allow high values for s in order to phenomenologically represent the dramatic increase of D for $C \gg C_{\text{perc}}$.

Framing the differential equation for diffusion-controlled growth meets with some mathematical difficulties that arise from the presence of concentration gradients surrounding the spherical sinks, as opposed to the zero-gradient incorporation-controlled case treated above. These problems are handled in Appendix B. The resulting differential equation for the precipitated fraction, which for the diffusion-controlled regime will be denoted by W_1^d, reads

$$-\frac{\ln(bW_1^d)dW_1^d}{(1-W_1^d)^{s+1}}=\frac{dt}{\tau_d}. \tag{14}$$

In contrast with the corresponding Eq. (9) for W_1^i, three rather than a single parameter appear in Eq. (14), viz. the power s, the dimensionless constant

$$b\equiv(3/4)(\pi n)^{1/2}vhC_{\text{in}}, \tag{15}$$

and the time constant

$$\tau_d\equiv\frac{s+1}{6\pi nD_0C_{\text{in}}^s}=\frac{s+1}{6\pi nD_{\text{in}}}. \tag{16}$$

In Eq. (16) the quantity

$$D_{\text{in}}\equiv D_0C_{\text{in}}^s[=D_{0A}C_{\text{in}}^s\exp(-E_{\text{diff}}/kT)] \tag{17}$$

represents the initial value of D; cf. Eq. (12). For whole values of $s>0$ and for $W_1^d(0)\approx 0$ the solution of differential equation (14) reads

$$s^{-1}\Bigg([1-(1-W_1^d)^{-s}]\ln(bW_1^d)-\ln(1-W_1^d)+\sum_{j=1}^{s-1}j^{-1}[(1-W_1^d)^{-j}-1]\Bigg)=t/\tau_d, \tag{18}$$

with the proviso that for $s=1$ the Σ term in this equation drops out.

All the values of the parameters on the right-hand side of Eq. (15) are known (see Sec. II), viz. $n=6\times10^{10}\ \text{cm}^{-2}$, $v=3.0\times10^{-23}\ \text{cm}^3$ and $hC_{\text{in}}=3.1\times10^{14}\ \text{cm}^{-2}$, which yields $b=3.0\times10^{-3}$. Normalized W_1^d-t/τ_d curves for this value of b and for s ranging from 0 to 50 are presented in Fig. 8.

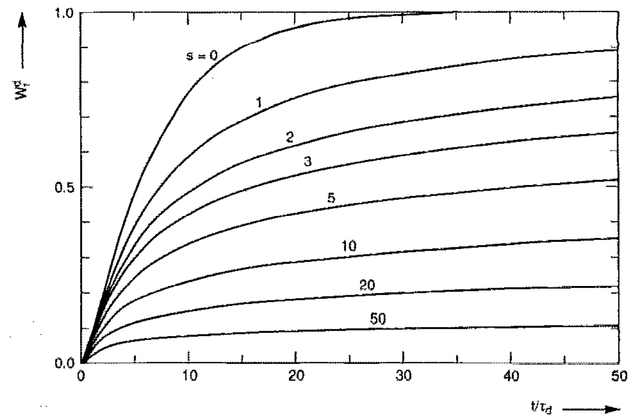

FIG. 8. The diffusion-controlled growth stage of precipitates: theoretical curves of the precipitated Sb fraction W_1^d vs the normalized annealing time, according to Eq. (18) with $b=3.0\times10^{-3}$ and for different values of s. The index 1 refers to simultaneous generation of nuclei; cf. caption of Fig. 7.

2. *Type (2): The growth of continuously generated nuclei*

The classical absolute-reaction-rate theory of Turnbull and Fisher[45,49] for surface-tension-controlled homogeneous nucleation in solids gives for the generation rate I of nuclei per unit of volume:

$$I=I_{0A}C\exp\left(-\frac{\Delta g+\Delta G_c}{kT}\right). \tag{19}$$

Here I_{0A} is a C- and T-independent frequency factor, Δg the activation energy for transfer of atoms across the surface of a nucleus, and ΔG_c the critical free energy for nucleation. Introducing for brevity I_0 given by

$$I_0\equiv I_{0A}\exp\left(-\frac{\Delta g+\Delta G_c}{kT}\right) \tag{20}$$

and substituting $C=C_{\text{in}}[1-W_2(t)]$, Eq. (19) becomes

$$I(t)=I_0C_{\text{in}}[1-W_2(t)]. \tag{21}$$

For a collection of precipitates with identical radii, like those of the type (1) of Sec. III B 1, one can make a distinct discrimination of the four stages of development, viz. nucleation, incorporation-controlled growth, diffusion-controlled growth, and Ostwald ripening. However, in the present case of continuous generation and the ensuing simultaneous presence of nuclei with different radii, this is not possible. After some time the older nuclei will already have passed into the diffusion-controlled stage, whereas the younger nuclei remain still in the incorporation-controlled stage. We shall restrict ourselves below to calculating $W_2^i(t)$ corresponding to the initial time interval when *all* supercritical nuclei are still in the incorporation-controlled stage.

Let us consider a particular nucleus that has become supercritical at the moment $t=\tau$. For calculating its volume $V(t,\tau)$ at the time t we assume that the diameters of the type (2) precipitate spheres remain smaller than h, resulting in a simple 3D problem. The following analogue of Eq. (7) is then derived easily:

$$V(t,\tau)=\frac{4\pi}{3}\left(vkC_{\text{in}}\int_\tau^t[1-W_2^i(t')]dt'\right)^3. \tag{22}$$

The expression for $W_2^i(t)$ reads

$$W_2^i(t)=(vC_{\text{in}})^{-1}\int_0^t I(\tau)V(t,\tau)d\tau. \tag{23}$$

Substituting here Eqs. (21) and (22) yields the nonlinear double-integral equation

$$W_2^i(\mathcal{T}_2)=\int_0^{\mathcal{T}_2}[1-W_2^i(\tau)]\times\left\{\int_\tau^{\mathcal{T}_2}[1-W_2^i(t')]dt'\right\}^3 d\tau, \tag{24}$$

where

$$\mathcal{T}_2\equiv t/\tau_{n2} \tag{25}$$

with the time constant τ_{n2} given by

$$\tau_{n2}\equiv[(4\pi/3)v^2I_0(kC_{in})^3]^{-1/4}. \tag{26}$$

The method of numerically solving Eq. (24) is given in Appendix A. The result is shown in Fig. 7. The most salient feature of the sigmoid $W_2^i - t$ curve, characteristic for continuous nucleation, is the "incubation time" before the precipitation becomes appreciable,[50,51] which time equals here roughly $0.4\tau_{n2}$.

IV. APPLICATION OF THE MODEL

We shall show now that the experimental curves of Figs. 3 and 4 can be assigned to a combination of processes of the types (1) and (2) treated in Sec. III.

A. Type I intervals

As can be seen from Fig. 2(a), the supposedly simultaneous generation of supercritical nuclei already has taken place during the SPE treatment. Formally this can be accounted for by introducing an additional annealing-temperature-dependent time interval $t_{SPE}(T)$ preceding the annealing process, an "SPE-induced equivalent annealing-time shift."

We assume that at the end of the incorporation-controlled growth stage W_1 is still negligible compared to its increase during the subsequent diffusion-controlled stage. If this is justifiable, we must be able to fit all five type I intervals in Fig. 4 with Eq. (18), and that using a single value for the adjustable parameter s and different values for $\tau_d(T)$ for each curve. Furthermore, we have to allow $t_{SPE}(T)$ as an additional adjustable parameter for each curve separately. Figure 8 demonstrates for that for $s\approx 20$ the theoretical curves exhibit an analogous "quasi-saturation" at $W\approx 0.2$ as the experimental data. The actual fitting will be performed in the first instance only to the 650 and 675 °C curves, which have three points in the diffusion-controlled regime, whereas the others have only two.

Due to the linearity in t of Eq. (18) one can use a simple direct procedure that enables making an allowance for the t_{SPE} time shifts. Rather than plotting the measured values of W_1^d itself vs t, as was done in Fig. 4, we plot now the values of the function of the left-hand side of Eq. (18) for these W_1^d values as the argument, again vs t. This is done for a number of whole values of s. It turns out then that the three data concerned for 650 °C are lying on a straight line—not through the origin—for the choice $s=25$. For the same value of s the three 675 °C data are also lying on a—different—straight line. The straight-line criterion is sufficiently sensitive to variations of a few units in

TABLE I. Experimentally determined values of the time constants τ_d [see Eq. (16)] and τ_{n2} [see Eq. (26)] and of the t_{SPE} time shifts (see Sec. IV A); for all temperatures $s=25$ [see Eq. (12)].

T(°C)	625	650	675	700	725
τ_d(s)	4.02	3.25	3.94	2.03	0.568
t_{SPE}(s)	54.3	25.0	32.0	24.3	1.92
τ_{n2}(s)	1367	911	370	56.8	7.32

s. From the slopes of the two straight lines one obtains the two values of τ_d, and from the cut-offs from the t axes those of t_{SPE}. These values are given in Table I.

In view of the overdeterminedness in the foregoing fitting (six data points in total for evaluating five parameters), its success constitutes a certain verification of the validity of the model. This is demonstrated more clearly in Fig. 9, where all six points are lying on a single $W-t/\tau_d$ curve. In this figure the t values for the two sets of data have been increased firstly with the corresponding t_{SPE} values and—in accordance with Fig. 8—were normalized subsequently to the corresponding τ_d values.

For the three remaining samples with only two points in the diffusion-controlled regime we also use $s=25$, which allows us to evaluate the two other adjustable parameters, $\tau_d(T)$ and $t_{SPE}(T)$, for each of them. All results are listed in Table I.

After all this, we can bring more order in the set of three upper curves of Fig. 6. Adding the $t_{SPE}(T)$-values of Table I to the t values and replotting yields the broken curves of Fig. 10. Though these corrected type I curves are now mutually parallel, they are no more straight than the type II curves. We shall come back to this problem in the first paragraph of Sec. V A.

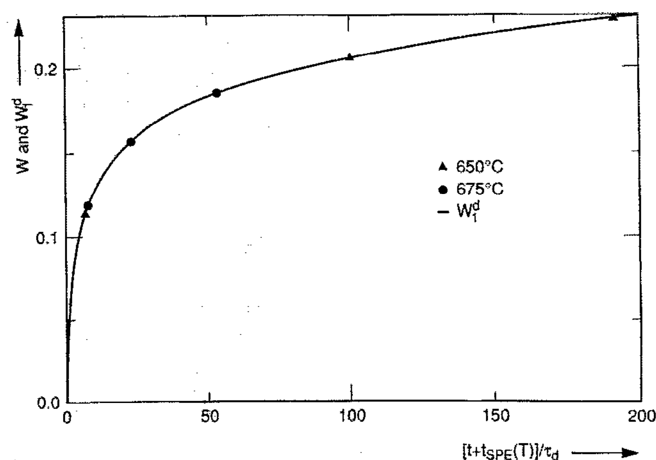

FIG. 9. The result of fitting the W_1^d curves of Fig. 8 to the six data points of the type I intervals (cf. Fig. 5) of the 650 and 675 °C curves of Fig. 4. Fitting is obtained for $s=25$ and for the values of $\tau_d(T)$ given in Table I. In this figure the experimental values for the six points have been increased with the pertinent $t_{SPE}(t)$ values of Table I and were normalized subsequently to the corresponding $\tau_d(T)$ values.

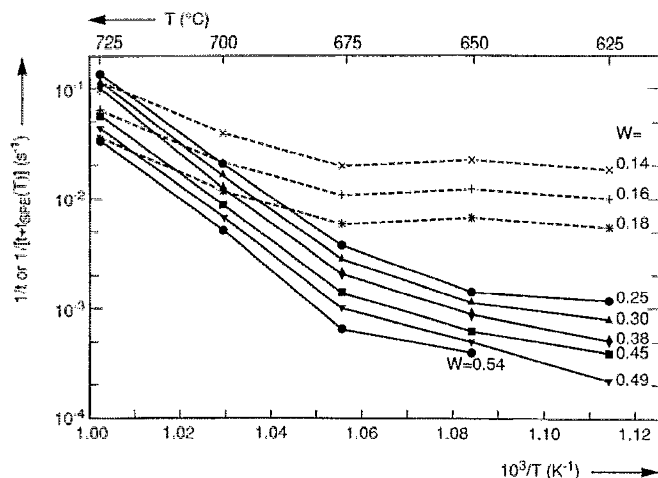

FIG. 10. Identical with Fig. 6, except that the type I (three upper) curves have been corrected by increasing their t values with the corresponding t_{SPE} values of Table I.

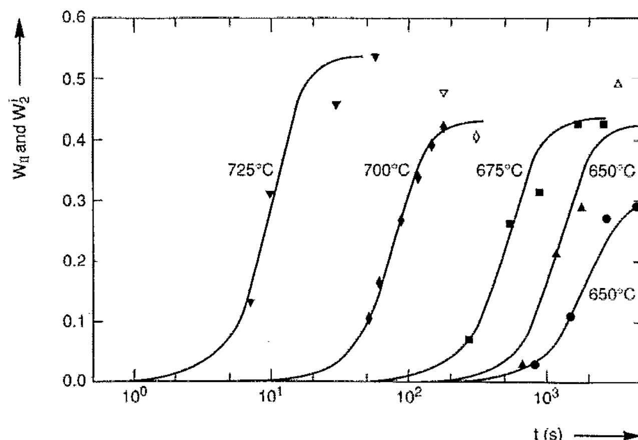

FIG. 11. The result of fitting the W_2^i curve of Fig. 7 to the processed data of the type II intervals of Fig. 4 (cf. Fig. 5). The processing consisted in applying Eq. (28) for finding $W_{II}(t)$ from the measured $W_{I+II}(t)$.

B. Type II intervals

The observed incubation time of the type II contributions in Fig. 4 [cf. $W_{II}(t)$ in Fig. 5] points to a type (2) process of continuous generation of nuclei. By trying to fit accordingly the $W_2^i(t)$ curve of Fig. 7 to our data we meet with the following problem.

In the region where the type (2) process starts to yield a significant contribution to W, or even where it dominates, the contribution of process (1) remains still non-negligible. Therefore, for the present fitting procedure one would like to firstly correct the data for contributions of the type (1) process. This is, however, unfeasible. The reason is the non-linearity of the complete integro-differential equation for parallel processes of the types(1) and (2). Strictly speaking, the solution of this complete equation should be fitted to all the data, but we shall follow a simplifying approach here.

For *linear* parallel processes characterized by individual precipitation functions $W_\alpha(t)$ and $W_\beta(t)$, the $W_{\alpha+\beta}(t)$ of the combined effect would be given by

$$W_{\alpha+\beta}(t)=W_\alpha(t)+W_\beta(t)-W_\alpha(t)\,W_\beta(t). \quad (27)$$

[Note that for $t\to\infty$ this gives the due result $W_{\alpha+\beta}(t)\to 1$ if $W_\alpha(t)\to 1$ and/or $W_\beta(t)\to 1$.] Equation (27) can be derived perspicuously by considering the electric analog of a charge condenser that is discharged through two parallel-connected resistors. The analog consists in that the time dependence of the charge fraction that is still present on the condenser is identical to that of the non-precipitated fraction $1-W_{\alpha+\beta}(t)$.

In spite of the nonlinearity of the present problem, yet we shall make use of Eq. (27); the resulting errors are difficult to estimate. The data points in the type II intervals in Fig. 4 corrected according to Eq. (27) are given by

$$W_{II}(t)=[W_{I+II}(t)-W_I(t)]/[1-W_I(t)], \quad (28)$$

where $W_{I+II}(t)$ represents the measured values, and the $W_I(t)$ were calculated from Eq. (18) using the parameter values found in Sec. IV A. The resulting points are shown in Fig. 11. Possible reasons for the saturation occurring already at $W_{II}(t)<1$ will be discussed in Sec. V C. For the fitting in Fig. 11 we have used the $W_2^i(t)$ curve of Fig. 7 with the ordinate values reduced in such a way that the resulting horizontal asymptote for $t\to\infty$ fits reasonably to the experimental point(s) with the highest W_{II} value(s) for the sample considered. [The reason for disregarding the points with the highest t values for 700 and 725 °C follows from item (ii) of Sec. V C.] The highest point for 650 °C is probably an aberration, as was already obvious from Fig. 3.

In contrast with the fitting of the type I curves, in the present case only a single parameter had to be adjusted for each sample, viz τ_{n2}. The values of τ_{n2} as found from the fitting shift along the logarithmic horizontal axis in Fig. 11 are given in Table I. The high values of τ_{n2} justify our omitting a correction of the type II curves with t_{SPE} values in an analogous way as performed for the type I curves. Figure 12(a) shows the $1/\tau_{n2}$ values in an Arrhenius plot.

V. DISCUSSION

In this section we discuss the final results for the type (1) and type (2) precipitation processes as summarized in the Arrhenius plots of Fig. 12. Further, possible reasons are given why the precipitation already stops at W values significantly below unity.

A. Vacancy-percolation diffusion

Figure 12(b) presents an Arrhenius plot of the diffusion coefficients calculated from the τ_d values of Table I (solid squares). The plotted values are those of D_{in}, which follow from the τ_d values by using Eq. (16) with $s=25$. The nonmonotonous course of these points, which is analogous to that of the three upper curves in Fig. 10, is unlikely to represent a real feature. In view of this and of the rather small accuracy of these corrected points, we make

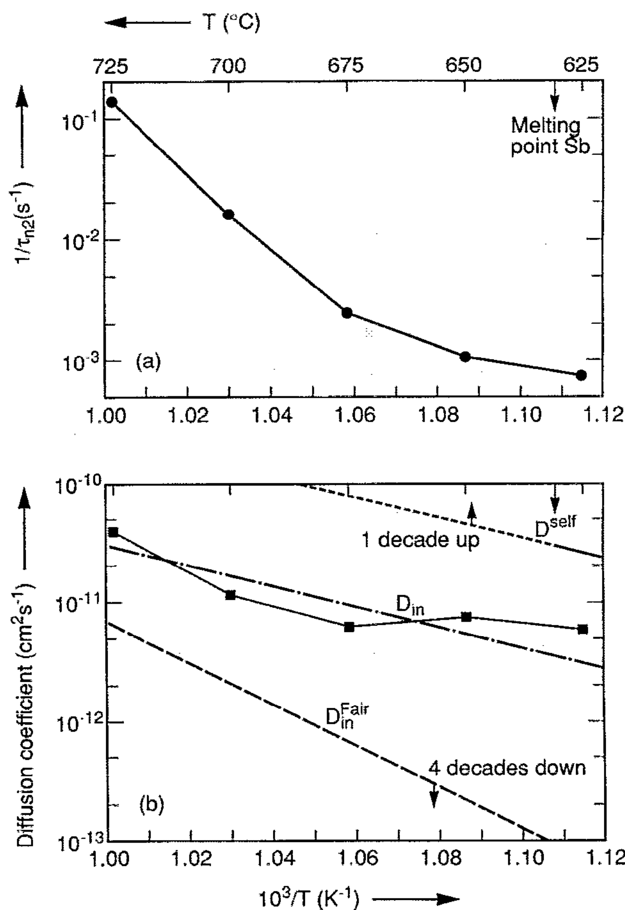

FIG. 12. Arrhenius plots for (a) the $1/\tau_{n2}$ values obtained from the fitting procedure shown in Fig. 11 and (b) the five D_{in} values calculated with the aid of Eq. (16) from the values of s and of the τ_d's obtained from the fitting procedure of Sec. IV A; the dot-and-dash line represents the rough average through these data given by Eq. (29). Also shown are: ···—the self-diffusion coefficient D^{self} in Sb, given by Eq. (30), - - -D^{Fair} given by Eq. (31), extrapolated to lower temperatures and to our initial $C_{in}=2.4\times10^{21}$ cm^{-3} to allow comparison with our D_{in} values. Note the vertical shifts to firstly be performed on the top and bottom lines before the values of D^{self} and D_{in}^{Fair} can be read from the given ordinate scale.

the rough approximation of representing them by the dot-and-dash straight-line average shown. This line is given by [cf. Eq. (17)]

$$D_{in}=D_{inA}\exp(-E_{diff}/kT)\quad[=D_{0A}C_{in}^{s}\exp(-E_{diff}/kT)]$$

with

$$D_{inA}=0.01\ \text{cm}^2/\text{s and } E_{diff}=1.7\ \text{eV}; \tag{29}$$

obviously, these values of D_{inA} and E_{diff} are very inaccurate. Yet it is interesting to compare this line[52] with the top and bottom straight lines in the same figure. The solid right-hand part of the top line represents the self-diffusion coefficient in solid, polycrystalline antimony.[53,54] The dotted part of the same line is an extrapolation to temperatures above the melting point of antimony (630.5 °C) and thus has no direct physical meaning. The equation for the line is given by[53,54]

$$D^{self}=D_A^{self}\exp(-E_{diff}^{self}/kT)$$

with

$$D_A^{self}=1.05\ \text{cm}^2/\text{s and } E_{diff}^{self}=1.73\ \text{eV}. \tag{30}$$

The bottom line in Fig. 12(b) was calculated from the following formula of Fair *et al.*[33,55] for the diffusion of Sb in Si:

$$D^{Fair}=D_{0A}^{Fair}C^2\exp(-E_{diff}^{Fair}/kT)$$

with

$$D_{0A}^{Fair}=1.37\times10^{-41}\ \text{cm}^8/\text{s and } E_{diff}^{Fair}=3.39\ \text{eV}. \tag{31}$$

Actually our use of this equation implies an extrapolation beyond its range of validity: the equation describes the experimental diffusion data considered in Ref. 33 for T between 1000 and 1200 °C, and for C near 2×10^{20} cm^{-3}. For calculating the D_{in}^{Fair} line in Fig. 12(b) we substituted our value

$$C_{in}=hC_{in}/h\approx3.1\times10^{14}/1.3\times10^{-7}=2.4\times10^{21}\ \text{cm}^{-3}$$

for C in Eq. (31), which gives a preexponential factor $D_{0A}^{Fair}C^2\approx80$ cm^2/s. Note that in the interval considered here our values of D_{in} lie on the average roughly 5 decades above those of D_{in}^{Fair} and only 2 decades below those of D^{self}.

An appropriate model for explaining our high D_{in} values may be based on the concept of vacancy-percolation diffusion,[32,35–39] the essentials of which were already summarized in Sec. I. However, we have some objections against the approach in Ref. 32 (which in its turn follows Refs. 35–38). Firstly, without due justification an effective diffusion coefficient D_{eff} for 3D diffusion has been introduced according to

$$D_{eff}=P_\infty D_{perc}+(1-P_\infty)D_{norm}. \tag{32}$$

Here P_∞ is the probability that a given Sb atom belongs to the "infinite" percolation cluster of high-diffusivity material (viz., silicon possessing fifth-neighbor Sb atoms; cf. Sec. I); D_{perc} and D_{norm} are the—concentration-dependent—diffusion coefficients of Sb in that cluster and in normal, lower-doped silicon, respectively. Equation (32) suggests a simple parallel connection of the infinite cluster of high-diffusivity material and an infinite cluster of normal material, without taking due account of the *finite* clusters of both materials, which are also present. Secondly, for describing the increase of P_∞ for an increase of C from the percolation-threshold concentration C_{perc} to $3C_{perc}$, a so-called critical exponent was used which in actual fact is applicable only up till $C\approx1.1\ C_{perc}$.[56,57]

A better approach to framing an expression for D_{eff}, starting from the same idea of a random mixture of high-diffusivity and normal materials, might proceed as follows. Let us start from the simplified, hypothetical case that the above-mentioned D_{perc} and D_{norm} are concentration *in*dependent. More specifically, we take $D_{norm}=0$, so that diffusion takes place by way of the percolation network of high-diffusivity material exclusively. The simplified percolation problem thus defined is exactly the familiar problem of "the ant in the labyrinth," the diffusion of a particle in

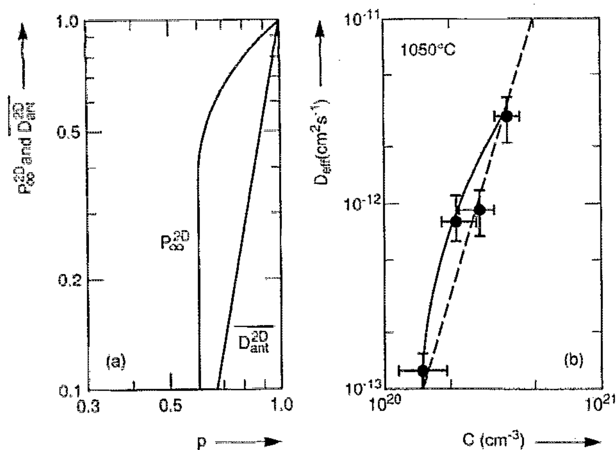

FIG. 13. (a) Theoretical curves for the percolation probability P_∞^{2D} and the normalized diffusivity, $\overline{D_{ant}^{2D}}$, for a disordered network on a 2D square lattice vs the site-occupation probability p; after Refs. 58 and 59 ($\overline{D_{ant}^{2D}}=1$ for $p=1$, i.e., for complete occupation). (b) —— the fitting in Ref. 32 of the expression for D_{eff} from the vacancy-percolation diffusion theory [Eq. (32)] to the Sb diffusion data of Ref. 30, - - - - - the fitting in Ref. 30 to the same data, using the power law of Eq. (12) with $s=3.6$. [For converting abscissa values from n/n_i to C ($\approx n$) we took n_i (1050 °C) $=10^{19}$ cm^{-3}.]

a disordered network (or the analogous problem of the conductivity of a random-resistor network).[58,59] Fortunately, for 2D geometries this problem has already been solved. The diffusion coefficient for this case will be denoted here as D_{ant}^{2D}. Figure 13(a) shows a double-logarithmic plot of $\overline{D_{ant}^{2D}}$, the normalized D_{ant}^{2D} for a 2D square lattice, versus the fraction p of the lattice sites that are "occupied," i.e., that provide diffusional (or conducting) pathways; see, e.g., Refs. 58 and 59. Our suggestion is that the $D_{eff}-C$ curve for Sb-diffusion in 2D δ layers might be obtained by properly modifying this $\overline{D_{ant}^{2D}}-p$ curve. To express D_{eff} as a modified D_{ant}^{2D} one has to try to bring into account the realistic, concentration-dependent D_{perc} and D_{norm} of Refs. 31 and 38. Furthermore, in a first approximation direct proportionality between C and p may be assumed. (An additional problem will be how to account for the effect of closer-than-fifth Sb neighbors.)

In the light of the last paragraph the inadequacy of the criticized 3D equation (32) can be presented now more perspicuously. For our simple case of constant D_{perc} and $D_{norm}=0$ this equation yields $D_{eff}\propto P_\infty$ rather than $D_{eff}=D_{ant}$, as would be correct. Though the exact shape of D_{ant}^{3D} vs p appears not to be known in the literature, it is plausible that it differs considerably from that of P_∞^{3D} vs p. This can be inferred from the great difference in the 2D case, where both curves are known; see Fig. 13(a).

More arguments for our objections can be extracted from Ref. 32, where the application of Eq. (32) to 3D Sb diffusion produced the solid $D_{eff}-C$ fitting curve of Fig. 13(b). As might already be conjectured from the last paragraph, this curve exhibits the same feature of concavity as the $P_\infty^{2D}-p$ curve of Fig. 13(a). Before publishing this concave fitting curve the same authors reported[30,31,34] that a purely phenomenological fit to the same experimental data was obtained with a straight line given by Eq. (12) with $s=3.6$; see the broken line in Fig. 13(b). Our present considerations and the near-straightness of the $\overline{D_{ant}^{2D}}-p$ curve of Fig. 13(a) appear to argue in favor of the original straight-line fit, against the concave one. This is further supported by the experimental results of the present work. Extrapolation of our Eq. (29) to the temperature of 1050 °C of Fig. 13(b) yields $D_{in}=3.6\times10^{-9}$ cm^2/s, corresponding to $C_{in}\approx2.4\times10^{21}$ cm^{-3}. This associated pair of values lies rather close to the extrapolation of the straight line in Fig. 13(b) and very far above any reasonable extrapolation of the curved line.

On closer inspection the above value of C_{in}, found by making use of $h=1.3$ nm, turns out not to be correct. When the Sb diffusion takes place *via* charged vacancies, D depends on the local electron concentration, since this concentration codetermines the local charged-vacancy concentration through a so-called quasi-chemical equilibrium condition.[33,60,61] The electrons, though they are confined in a two-dimensional quantum well with a thickness of the order of some nm,[1,4,8,11,12,15] are still significantly extending beyond the Sb-layer with thickness h. The ensuing broadening of the layer with high diffusivity will bring about some fast initial perpendicular Sb diffusion, until the sloping Sb profile nearly coincides with that of the electrons. Formally this initial outdiffusion of the δ layer can roughly be accounted for by using a lower value of C_{in}. This implies that our data point at the end of the preceding paragraph shifts to the left, so that it will lie even considerably *above* the extrapolated straight line. Thus for increasing C the slope even increases, which is consistent with our finding of $s\approx25$ at $C=C_{in}$. Finally, a lower value of C_{in} will also entail a lowering of the D_{in}^{Fair} line in Fig. 12(b).

In spite of all uncertainties, in our view the concept of vacancy-percolation diffusion still provides the best available basis for developing a quantitative theory for the diffusion of a number of impurities in δ layers.

B. The type (2) nucleation and growth

Examination of the $\ln(1/\tau_{n2})$ vs $1/T$ curve of Fig. 12(a) raises the question about the origin of the variation of its slope with as much as a factor of 6. Let us start by inspecting the expression for τ_{n2} of Eq. (26), where I_0 is given by Eq. (20). In the latter equation, neglecting elastic-energy contributions, ΔG_c is given by[45] $\Delta G_c=(4\pi/3)R_c^2\sigma$, where σ is the surface free energy per unit of area and where the radius R_c of the critical nucleus is given by[45] $R_c=2\sigma v/kT\ln(C/C_s)$. Thus we find for $\Delta G_c/kT$:

$$\frac{\Delta G_c}{kT}=\frac{16\pi}{3}\left(\frac{\sigma}{kT}\right)^3\left(\frac{v}{\ln(C/C_s)}\right)^2. \quad (33)$$

In this equation we substitute $C\approx C_{in}=2.4\times10^{21}$ cm^{-3}. Further we take $T=725$ °C; extrapolation of an expression in Ref. 28 to this value of T gives $C_s=5.6\times10^{18}$ cm^{-3}. Finally, σ is generally[45] of the order of 100 erg cm^{-2} (cf. Ref. 29). With all this we find $\Delta G_c/kT=0.16$. When substituting accordingly $\exp(-\Delta G_c/kT)\approx1$ in Eq. (20), one

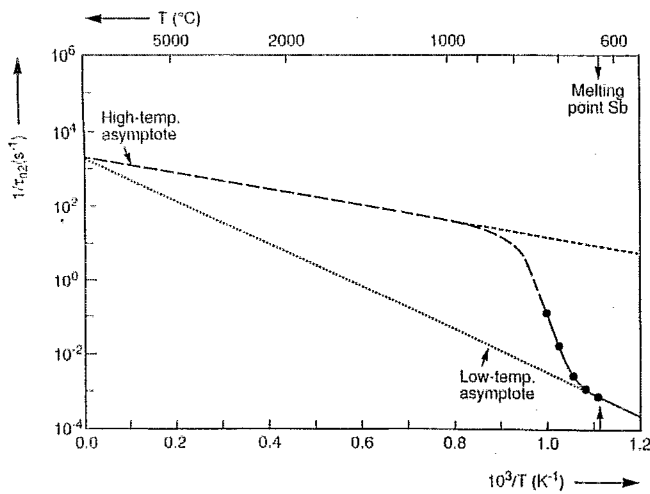

FIG. 14. A possible explanation for the curvature of the $1/\tau_{n2}$ vs $1/T$ curve of Fig. 12(a). Different values of E_{surf} for Sb atom incorporation into solid and liquid Sb-precipitates will produce different slopes of the low- and high-temperature asymptotes.

obtains the following expression for I_0, which may well be in error with a good few orders of magnitude:

$$I_0 \approx I_{0A} \exp\left(-\frac{\Delta g}{kT}\right) = I_{0A} \exp\left(-\frac{E_{surf}}{kT}\right). \quad (34)$$

We have also made use here of the identicalness of Δg and E_{surf}, which follows from comparing the definition of Δg, given after Eq. (19), with that of E_{surf}, given implicitly in Eq. (4). By substitution of Eqs. (4) and (34) in (26), this equation can be rewritten finally as

$$1/\tau_{n2} \approx [(4\pi/3)v^2 I_{0A}(k_A C_{in})^3]^{1/4} \exp(-E_{surf}/kT). \quad (35)$$

Differentiation of this equation—leaving open the possibility that E_{surf} depends on T—yields for the slope in question:

$$|\text{slope}| \equiv -\frac{d \ln(1/\tau_{n2})}{d(1/T)} \approx \frac{1}{k}\left(E_{surf} - T\frac{dE_{surf}}{dT}\right). \quad (36)$$

Thus a variation of the slope may result from a variation of E_{surf} with T.

Figure 14 shows a possible but quantitatively largely arbitrarily chosen "switch-over" continuation of the experimental curve, for which E_{surf} decreases with increasing T up to approximately 850 °C, after which it becomes constant again. We suggest ascribing the decrease of E_{surf} with T to the precipitates passing beyond the Sb melting point. The observed gradual rather than abrupt switch-over would indicate then a certain distribution of the rise of the melting point in the precipitates, which can be brought about by different degrees of pressure increase for the different sizes.

There is some additional support for the suggestion that the steep part of the slope corresponds indeed with a switch-over phenomenon (from Sb incorporation into solid precipitates to incorporation into liquid ones), rather than with a single process. For the latter case the steep slope would yield 6.6 eV for E_{surf}, which seems implausibly high. More decisively, the corresponding value of the prefactor, roughly 10^{33} s^{-1} (as found from extrapolation to $1/T=0$ in Fig. 14), is very many decades higher than expected from Eq. (35), which is seen as follows. The theory of absolute reaction rates[49,62,63] shows that $k_A \approx aI_{0A}$, where a represents a lattice parameter and I_{0A} equals an atomic vibration energy ($a \approx 3$ nm and $I_{0A} \approx 10^{13}$ s^{-1}). Substitution in Eq. (35) yields for the prefactor, within a few orders of magnitude, a value of only 2×10^{10} s^{-1}. (This value corresponds within an order of magnitude to that found from the extrapolation of a straight line through the 650 and 675 °C data points of Fig. 14, which gives roughly 10^{11} s^{-1}. The slope of this line would yield $E_{surf} \approx 2.8$ eV. However, this rough correspondence of prefactor values, which would throw doubt on the reliability of the 625 °C point, may well be fortuitous.)

Summarizing this section: in principle the observed super-exponential increase of $1/\tau_{n2}$ with decreasing $1/T$ can be explained by an increasing fraction of liquid precipitates with a much lower value of E_{surf} than the solid ones.

C. Incompleteness of precipitation

Since the ratio C_{in}/C_s equals at least 430 [see the values given below Eq. (33)], one might expect W to finally approximate practically unity. However, W appears to saturate (or occasionally to decrease again) already at $W=0.45$–0.65; see Fig. 3. Possible explanations for this are as follows:

(i) For sufficiently reduced C values the very small perpendicular diffusion will not be completely dominated any more by the lateral diffusion. The perpendicular diffusion withdraws Sb atoms from the precipitation process. Moreover, the perpendicular diffusion will lower the value of W at which the condition $C/C_s \gg 1$ in the δ layer will not be satisfied any more. According to Eq. (33), a still further decrease of C entails then non-negligibility of $\Delta G_c/kT$. In its turn this causes a fast decrease of I [cf. Eq. (19)], so that the generation of fresh type (2) nuclei will exhibit an almost abrupt stop.

(ii) Dissolution of the smaller type (2) precipitates might take place. The released Sb atoms may not be trapped—as in 3D Ostwald ripening—by the type (1) and the larger type (2) precipitates (cf. second paragraph of Sec. III B and Ref. 29), but diffuse away from the δ layer, as under (i). Such a process would also explain the occasionally observed final decrease of W.

(iii) The saturation value of the actual fraction precipitated, rather than being 0.45–0.65, might be closer to 1.0 if the precipitates are partly coherent in the Si lattice and thus indetectable with RBS.

VI. CONCLUSIONS

The study of δ layers in silicon turns out to be interesting not only for device applications, but also because it allows the basic investigation of diffusion and precipitation processes up till much higher impurity concentrations than

reachable by 3D doping. For Sb δ layers the interpretation of RBS minimum-yield data in terms of lateral diffusional transport followed by precipitation has provided here information on the underlying mechanisms. The characteristic features of these data for samples annealed at 625–725 °C can be explained by postulating two parallel mechanisms of precipitation.

(i) Fast, simultaneous generation of a limited number of nuclei, the growth of which reaches rapidly the diffusion-controlled regime. This produces the precipitates observed on TEM pictures. The nucleation already occurs during the SPE stage and takes place probably at a limited number of certain low-energetic sites in the δ plane ("heterogeneous nucleation"). The diffusion coefficient describing the Sb diffusion towards the precipitates is a very strongly increasing function of the Sb concentration. This 2D-diffusion behavior can probably be described quantitatively by adapting the 3D vacancy-percolation diffusion model of Refs. 32 and 35–39.

(ii) Slow, continuous generation of hypothetical nuclei with subsequent incorporation-controlled growth. The resulting precipitates (diameter <1 nm) are invisible on TEM pictures. The annealing time needed for producing a significant amount of precipitation entails here an incubation period and a sigmoid shape of the W vs t curve. The slow nucleation may take place at numerous random non-low-energetic sites in the δ plane, due to statistical density fluctuations of the Sb atoms ("homogeneous nucleation"). The observed strong acceleration of the precipitation rate with increasing temperature can be explained by an increasing fraction of liquid precipitates with a considerably lower activation energy for Sb incorporation than solid ones.

ACKNOWLEDGMENTS

The authors thank C. W. T. Bulle-Lieuwma and D. W. E. Vandenhoudt for the TEM analysis and E. P. Naburgh for the RBS measurements.

APPENDIX A: SOLUTION OF INTEGRAL EQUATIONS

For solving the integral equation (9) we use the method of successive approximations. Thus we construct a sequence of successive functions

$$W_1^{i(0)}(\mathcal{T}_1),\ W_1^{i(1)}(\mathcal{T}_1),\ W_1^{i(2)}(\mathcal{T}_1),\ldots,W_1^{i(n)}(\mathcal{T}_1),\ldots$$

by means of the recursive relation

$$W_1^{i(n+1)}(\mathcal{T}_1)=\left(\int_0^{\mathcal{T}_1}[1-W_1^{i(n)}(t')]dt'\right)^{3/2}, \qquad (A1)$$

where we start with $W_1^{i(0)}(\mathcal{T}_1)\equiv 0$.

In applying Eq. (A1) for finding $W_1^{i(m)}$, the result of analytic integration is series expanded in powers of $\mathcal{T}_1^{3/2}$ and cut off after the mth term. The result is that every repeated application of Eq. (A1) adds another higher-order term to the unchanged previous approximation. After four applications this yields

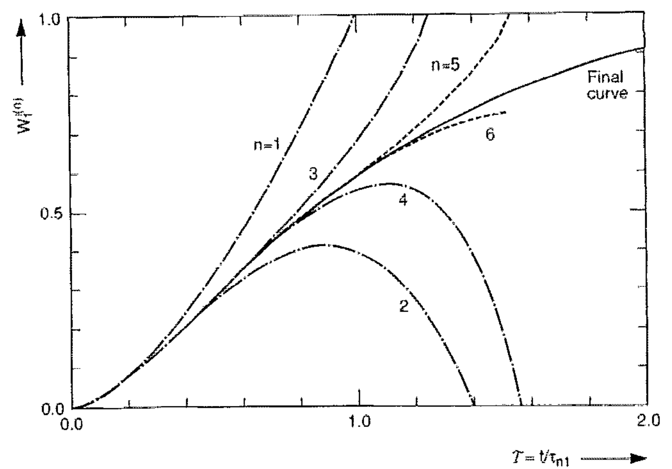

FIG. 15. The successive approximations $W_1^{i(n)}(\mathcal{T}_1)$ to the function $W_1^i(\mathcal{T}_1)$ as calculated with the aid of Eq. (A1): (1)–(4) results of the first four analytical integrations with starting function $W_1^{i(0)}(\mathcal{T}_1)\equiv 0$; (5)–(6) results of the next two numerical integrations. The solid line represents the final curve.

$$W_1^{i(4)}(\mathcal{T}_1)=\mathcal{T}_1^{3/2}(1-0.6000\mathcal{T}_1^{3/2}+0.2850\mathcal{T}_1^{6/2}-0.1227\mathcal{T}_1^{9/2}). \qquad (A2)$$

The successive results for $n=1$–4 are plotted in Fig. 15. We continue the sequence of approximations using numerical integrations in applying Eq. (A1). This is also done four times, giving the curves for $n=5$–8. In Fig. 15 only the curves for $n=5$ and 6 are shown, since those for $n=7$ and 8 turn out to practically coincide—over the range calculated, i.e., up to $\mathcal{T}_1\approx 1.5$—with the final curve represented by the solid line. This final curve was found as follows.

It turned out that in the interval $1.0<\mathcal{T}_1<1.5$ the curve for $n=8$ can be described very accurately by the heuristic function

$$W_1^i=1-\kappa\exp(-\lambda t)$$

with

$$\kappa=1.5312 \quad \text{and} \quad \lambda=1.3321. \qquad (A3)$$

Two further applications on Eq. (A1) lead to virtually identical reproductions of this "final" function up to as far as $\mathcal{T}_1=3.0$.

An analogous approach was followed in solving the double-integral equation (24). For W_2^i we only show the final result, again in Fig. 7.

APPENDIX B: DIFFUSION-CONTROLLED GROWTH

In case of incorporation-controlled growth of the type (1) process the diffusion coefficient is large enough to maintain the lateral Sb diffusion towards the spherical precipitates with only negligible concentration gradients. This quasi-homogeneity of the concentration in the δ plane (outside the precipitates) entails linear additivity of the individual Sb incorporation rates into the—in this case identical—spheres. Consequently, the total precipitation

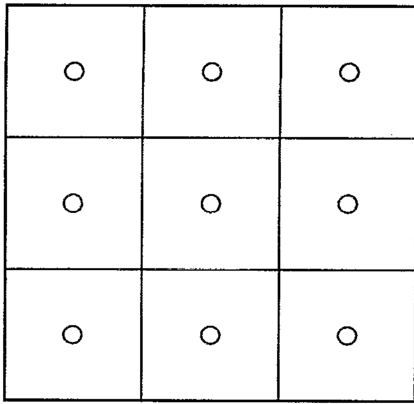

FIG. 16. A simple square periodic lattice of spherical precipitates, divided into square cells; after Ham.[64]

rate per unit of area can be found from the rate for a single sphere, viz. by multiplying with the sphere density n; cf. Eqs. (7) and (8). Obviously the exact spatial distribution of the spheres over the δ plane is irrelevant here.

On the other hand, for diffusion-controlled growth the concentration gradients are essentially non-negligible. The concentration profile depends on the density distribution of the spheres over the plane, which impedes an exact solution. The case of $s=0$ in Eq. (12) for D has been treated by Ham,[64] both for 2D and 3D geometries, by introducing the approximation of a *regular* spatial array of spheres, which enables the application of eigenfunction methods. For $s\neq 0$, however, the regular-array approximation generally is of no great use, since eigenfunction methods do not exist then.[65] Now it is a fortunate circumstance that, in spite of lack of eigenfunction methods, the regular-array approximation becomes useful again for our very high values of s ($s\approx 25$; see Sec. IV A). This can be shown as follows.

Let us consider a simple square periodic lattice of spheres. This lattice is divided into equivalent symmetrical square cells centered around each particle; see Fig. 16. We shall start by trying to find a sufficiently accurate solution for a single cell in this lattice. For this purpose we adopt another of Ham's approximations,[64] viz. that of replacing the square cell by a circle of equivalent area, i.e., with a radius r_0 defined by

$$\pi r_0^2 n = 1. \tag{B1}$$

As a consequence, the diffusional Sb supply to the ring-shaped surface of the slice with thickness h cut out from the sphere by the δ layer, possesses cylindrical symmetry. Therefore the continuity equation in the case of $D=D_0C^s$ reads

$$\frac{\partial C}{\partial t}=\frac{1}{r}\frac{\partial}{\partial r}\left(D_0C^s r\frac{\partial C}{\partial r}\right). \tag{B2}$$

We shall follow here the usual steady-state approximation,[45,47,64,66] through which Eq. (B2) simplifies to the ordinary differential equation

$$\frac{1}{r}\frac{d}{dr}\left(D_0C^s r\frac{dC}{dr}\right)=0. \tag{B3}$$

Since the solid solubility of Sb in Si for $T<725\,^\circ\mathrm{C}$ is less than $2\times 10^{-3}\,C_{\mathrm{in}}$ [see under Eq. (33)], it is allowed to set $C=0$ for the boundary condition at the slice surface:

$$C=0 \quad \text{for } r=R. \tag{B4}$$

With this, the solution of Eq. (B3) becomes

$$C(r)=G\left[\frac{s+1}{D_0}\ln\left(\frac{r}{R}\right)\right]^{1/(s+1)}. \tag{B5}$$

Strictly speaking, the constant G has to be determined from the other boundary condition, at the outer cell boundary:

$$\frac{dC}{dr}=0 \quad \text{for} \quad r=r_0. \tag{B6}$$

Differentiation of Eq. (B5) yields for the derivative

$$\frac{dC}{dr}=\frac{G^{s+1}}{D_0C^s r}. \tag{B7}$$

Application of Eq. (B6) thus yields the trivial solution $G=0$. This problem can be circumvented by the following alternative approach, in which the constant G is maintained provisionally.

The growth of the sphere radius R with t follows from the analogue of Eq. (5):

$$\frac{1}{v}\frac{dV}{dt}=\frac{1}{v}\frac{d}{dt}\left(\frac{4\pi R^3}{3}\right)=2\pi rhD_0C^s\frac{dC}{dr}. \tag{B8}$$

The right-hand side of this equation represents the diffusional Sb-atom flux to the sphere, which is independent of r in the steady-state approximation. Substitution of Eq. (B7) in (B8) and subsequent elimination of G with the aid of Eq. (B5) yields

$$R^2dR=\frac{vhD_0C^{s+1}(r,t)}{2(s+1)\ln(r/R)}dt. \tag{B9}$$

In accordance with the principle of steady-state approximating we have reintroduced here the dependence of C on t. Due to the above-mentioned r independence of the flux, Eq. (B9) is valid for all r between R and r_0. We make the choice $r=r_0$ and shall calculate the value of $C^{s+1}(r_0,t)/\ln(r_0/R)$ figuring at the right-hand side of Eq. (B9)

To the above end we shall show first that the shape of the function $C(r)$ given by Eq. (B5) with nonzero G represents a close approximation to the exact concentration profile. The function of Eq. (B5) is presented in Fig. 17 in a normalized plot of $C(r)/C(r_0)$ vs r/R. For the parameter values in this figure we have chosen $s=0$, 2, and 25, and $r_0/R=10$ and 20. In the course of our annealing experiments the ratio r_0/R approaches the final rough value of 10 from the side of higher values. Though for $s=25$ and $r_0/R=10$ the derivative dC/dr at $r=r_0$ does not exactly satisfy Eq. (B6), Fig. 17 shows that the relevant, *relative* value of the derivative is very small. Thus Eq. (B5) with

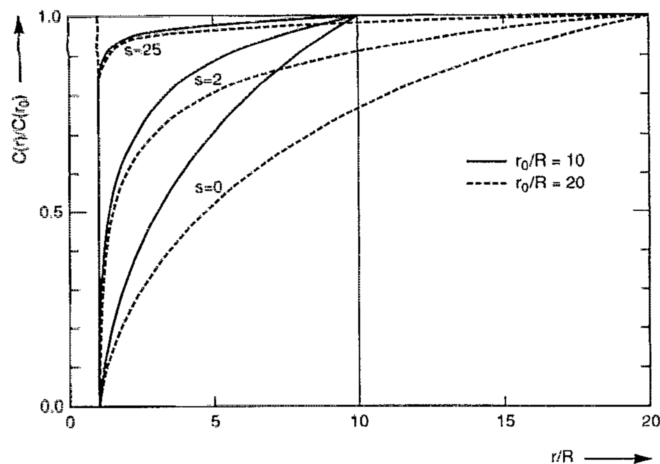

FIG. 17. Diffusion-controlled growth of the precipitates: normalized plot of the Sb concentration vs the distance to the center of the precipitate when only a single precipitate is present, as given by Eq. (B5). R represents the radius of the sphere. $C(r)$ has been normalized to its value $C(r_0)$ on the circular boundary defined by Eq. (B1). The parameter values chosen are $s=0$, 2, and 25, and $r_0/R=10$ and 20.

$s=25$ represents indeed a good approximation to the exact concentration profile with zero derivative at $r=r_0$.

Next, from the curve for $s=25$ and $r_0/R=10$ of Fig. 17 it can be calculated that $C(r_0,t)$ is only slightly larger than the areal-averaged concentration $\overline{C}(t)$: their relative difference amounts to only 2%. Thus, after substituting $r=r_0$ into Eq. (B9), and making subsequent use of $C(r_0,t) \approx \overline{C}(t)$ and of Eq. (B1) we obtain

$$\ln(\sqrt{\pi n}R)R^2dR \approx -\frac{vhD_0\overline{C}^{s+1}(t)}{2(s+1)}\,dt. \tag{B10}$$

Finally, this equation can be transformed into the differential equation (14) for the precipitated fraction W_1^d by substituting R from $W=4\pi R^3 n/3vhC_{\rm in}$, and $\overline{C}=C_{\rm in}(1-W_1^d)$.

[1] A. A. van Gorkum, K. Nakagawa, and Y. Shiraki, J. Appl. Phys. **65**, 2485 (1989).
[2] A. A. van Gorkum and K. Yamaguchi, IEEE Trans. Electron Devices **ED-36**, 410 (1989).
[3] K. Nishi, K. Sakamoto, and J. Ueda, J. Appl. Phys. **59**, 4177 (1986).
[4] G. Tempel, F. Koch, H. P. Zeindl, and I. Eisele, J. Phys. **48**, C5-259 (1987).
[5] H. Jorke, H. Kibbel, F. Schäffler, A. Casel, H.-J. Herzog, and E. Kasper, Appl. Phys. Lett. **54**, 819 (1989).
[6] W. F. J. Slijkerman, P. M. Zagwijn, J. F. van der Veen, A. A. van Gorkum, and G. F. A. van de Walle, Appl. Phys. Lett. **55**, 963 (1989).
[7] H.-M. Li, W.-X. Ni, M. Willander, K.-F. Berggren, B. E. Sernelius, and G. V. Hansson, Thin Solid Films **183**, 331 (1989).
[8] H.-J. Gossman, E. F. Schubert, D. J. Eaglesham, and M. Cerullo, Appl. Phys. Lett. **57**, 2440 (1990).
[9] S. Fukatsu, S. Kubo, Y. Shiraki, and R. Ito, Appl. Phys. Lett. **58**, 1152 (1991).
[10] S. Fukatsu, S. Kubo, Y. Shiraki, and R. Ito, J. Cryst. Growth **111**, 843 (1991).
[11] I. Eisele, Appl. Surf. Sci. **36**, 39 (1989).
[12] I. Eisele, Superlattices and Microstructures **6**, 123 (1989).
[13] H. P. Zeindl, G. Tempel, B. Bullemer, and I. Eisele, J. Electrochem. Soc. **88**, 515 (1987).
[14] H. P. Zeindl, T. Wegehaupt, I. Eisele, H. Oppolzer, H. Reisinger, G. Tempel, and F. Koch, Appl. Phys. Lett. **50**, 1164 (1987).
[15] H. P. Zeindl, T. Wegehaupt, and I. Eisele, Thin Solid Films **184**, 21 (1990).
[16] L. J. van IJzendoorn, C. W. Fredriksz, C. van Opdorp, D. J. Gravesteijn, D. W. E. Vandenhoudt, and G. F. A. van de Walle, Nucl. Instrum. Methods B **64**, 120 (1992).
[17] The *quantitative* values of the diffusion coefficient presented in Refs. 9 and 10 are dubious. The reason is that the application of the method presented by M. Ghezzo [J. Electrochem. Soc. **119**, 977 (1972)] (referred to incorrectly as "the Boltzmann–Matano analysis" in Refs. 9 and 10) is not justified due to different initial conditions. Moreover, Ghezzo's treatment is open to objections.
[18] A. P. Pogany, T. Preuss, K. T. Short, H. K. Wagenfeld, and J. S. Williams, Nucl. Instrum. Methods **209/210**, 731 (1983).
[19] A. Nylandsted Larsen, F. T. Pedersen, G. Weyer, R. Galloni, and A. Armigliato, J. Appl. Phys. **59**, 1908 (1986).
[20] T. Brabec, M. Schrems, M. Budil, H. W. Poetzl, W. Kuhnert, P. Pongratz, G. Stingeder, and M. Grasserbauer, J. Electrochem. Soc. **136**, 1542 (1989).
[21] S. J. Pennycook, J. Narayan, and O. W. Holland, J. Appl. Phys. **55**, 837 (1984).
[22] S. J. Pennycook, J. Narayan, and O. W. Holland, J. Cryst. Growth **70**, 597 (1984).
[23] S. J. Pennycook and R. J. Culbertson, Mat. Res. Soc. Symp. Proc. **52**, 37 (1986).
[24] S. J. Pennycook, R. J. Culbertson, and J. Narayan, J. Mater. Res. **1**, 476 (1986).
[25] S. J. Pennycook and R. J. Culbertson, Mat. Res. Soc. Symp. Proc. **74**, 379 (1987).
[26] S. J. Pennycook and R. J. Culbertson, Mat. Res. Soc. Symp. Proc. **100**, 411 (1988).
[27] S. J. Pennycook, Mat. Res. Soc. Symp. Proc. **147**, 45 (1989).
[28] D. Nobili, R. Angelucci, A. Armigliato, E. Landi, and S. Solmi, J. Electrochem. Soc. **136**, 1142 (1989).
[29] S. Solmi, F. Baruffaldi, and M. Derdour, J. Appl. Phys. **71**, 697 (1992).
[30] P. E. Andersen, A. Nylandsted Larsen, P. Tidemand-Petersson, and G. Weyer, Appl. Phys. Lett. **53**, 755 (1988).
[31] A. Nylandsted Larsen, P. E. Andersen, P. Gaiduk, and K. Kyllesbech Larsen, Mat. Sci. Eng. **B4**, 107 (1989).
[32] K. K. Larsen and A. N. Larsen, Mat. Sci. Forum **65-66**, 293 (1990).
[33] R. B. Fair, M. L. Manda, and J. J. Wortman, J. Mater. Res. **1**, 705 (1986).
[34] A. Nylandsted Larsen, P. Tidemand-Petersson, and P. E. Andersen, Inst. Phys. Conf. Ser. **95**, 499 (1989).
[35] D. Mathiot and J. C. Pfister, J. Phys. Lett. **43**, L453 (1982).
[36] D. Mathiot and J. C. Pfister, Physica B **116**, 95 (1983).
[37] D. Mathiot and J. C. Pfister, J. Appl. Phys. **55**, 3518 (1984).
[38] D. Mathiot and J. C. Pfister, J. Appl. Phys. **66**, 970 (1989).
[39] K. Kyllesbech Larsen, P. Gaiduk, and A. Nylandsted Larsen, Mat. Res. Soc. **163**, 601 (1989).
[40] M. Yoshida, Jpn. J. Appl. Phys. **10**, 702 (1971).
[41] S. M. Hu, Phys. Status Solidi B **60**, 595 (1973).
[42] A. A. van Gorkum, G. F. A. van de Walle, R. A. van de Heuvel, D. J. Gravesteijn, and C.W. Fredriksz, Thin Solid Films **184**, 207 (1990).
[43] C. Schiller (private communication).
[44] Leonard C. Feldman, James W. Mayer, and S. Thomas Picraux, *Materials Analysis by Ion Channeling* (Academic, New York, 1982), p. 59.
[45] J. W. Christian, *The Theory of Transformations in Metals and Alloys* (Pergamon, Oxford, 1965), Chap. X.
[46] O. Penrose, in *Stochastic Processes in Nonequilibrium Systems*, edited by L. Garrido, P. Seglar, and P. S. Shepherd (Springer, New York, 1978), p. 210.
[47] P. Haasen, *Physical Metallurgy* (Cambridge University Press, Cambridge, 1986).
[48] J. A. Marqusee and J. Ross, J. Chem. Phys. **79**, 373 (1983).
[49] D. Turnbull and J. C. Fisher, J. Chem. Phys. **17**, 71 (1949).
[50] W. A. Johnson and R. F. Mehl, Trans. Am. Inst. Mining Met. Engrs. **135**, 416 (1939).
[51] J. W. Christian, *The Theory of Transformations in Metals and Alloys* (Pergamon, Oxford, 1965), Chaps. I and XII.
[52] From the dot-and-dash average line in Fig. 12(b) one reads $D_{\rm in} \approx 5 \times 10^{-12}$ cm²/s for $T=650$ °C. In Sec. I we found a value as low as $D \approx r_0^2/t \approx 2\times 10^{-15}$ cm²/s from a very rough provisional estimate, where we took $t=2000$ s for the diffusion time needed for Sb depletion of the δ layer. According to the present model we should rather take

$t=700$ s, corresponding to the quasi-final value $W \approx 0.2$ or $C \approx 0.8\ C_{in}$ (the quasi-saturation level of the type I curves; see Figs. 4 and 5). This gives the still very rough estimate $D \approx 6 \times 10^{-15}$ cm^2/s, representing a kind of average of D over the range from C_{in} to 0.8 C_{in}. Over this range D varies from the value D_{in} mentioned above to a quasi-final value which, according to Eq. (12) with (17), equals $D \approx 0.8^{25} \times 5 \times 10^{-12} = 2 \times 10^{-14}$ cm^2/s. Since D_{in} exceeds by far the quasi-final D value, the average D will lie close to the latter, "bottle-neck" value. The fact that our estimated average D of 6×10^{-15} cm^2/s is even a factor of three lower than the quasi-final D of 2×10^{-14} cm^2/s is assignable to the very rough estimating method.

[53] A. Hässner and R. Hässner, Phys. Status Solid **11**, 575 (1965).

[54] P. P. Kuz'menko and G. P. Grinevich, Diffusion and Defect Data **9**, 190 (1974).

[55] Equation (31) is not given here in the usual general form, in which the intrinsic free-charge-carrier concentration n_i figures. The reason is lack of consensus concerning the exact definition of n_i. The only influence of n_i on the diffusion coefficient is through the electric-field term. Since for our extremely high C values this influence becomes completely negligible, the ambiguity is avoided here by using Eq. (31), which does not contain n_i. This equation gives a perfectly adequate description of Fair's asymptotic $D \propto C^2$ intervals for his different temperatures.

[56] D. Stauffer, *Scaling Theory of Percolation Clusters* (North-Holland, Amsterdam, 1979).

[57] J. Hoshen, D. Stauffer, H. Bishop George, Ralph J. Harrison, and George D. Quinn, J. Phys. A, Math. Gen. **12**, 1285 (1979).

[58] P. G. de Gennes, La Recherche **7**, 919 (1976).

[59] Dietrich Stauffer, *Introduction to Percolation Theory* (Taylor and Francis, London, 1985).

[60] Richard B. Fair, in *Impurity Doping*, edited by F. F. Y. Wang (North-Holland, Amsterdam, 1981), p. 315.

[61] P. M. Fahey, P. B. Griffin, and J. D. Plummer, Rev. Mod. Phys. **61**, 289 (1989).

[62] Keith J. Laidler, *Chemical Kinetics* (Tata McGraw Hill, New Delhi, 1983).

[63] J. W. Christian, *The Theory of Transformations in Metals and Alloys* (Pergamon, Oxford, 1965), Chap. III.

[64] Frank S. Ham, J. Phys. Chem. Solids **6**, 335 (1958).

[65] In Ref. 29 the authors have applied Ham's approach of Ref. 64 unjustifiably in view of the concentration-dependent contribution to D (viz. with $s=2$) used by them.

[66] C. Wert and C. Zener, J. Appl. Phys. **21**, 5 (1950).